Co-electrolysis of H_2O and CO_2 on exsolved Ni nanoparticles for efficient syngas generation at controllable H_2/CO ratios

V. Kyriakou[a,*], D. Neagu[b], E.I. Papaioannou[b], I.S. Metcalfe[b], M.C.M. van de Sanden[a,c], M.N. Tsampas[a]

[a] *Dutch Institute for Fundamental Energy Research (DIFFER), 5612 AJ Eindhoven, the Netherlands*
[b] *School of Engineering, Newcastle University, UK*
[c] *Department of Applied Physics, Eindhoven University of Technology, 5600 MB Eindhoven, the Netherlands*

A B S T R A C T

Syngas ($CO + H_2$) is a key-intermediate for the production of liquid fuels via the Fischer-Tropsch process. An emerging technology for generating syngas is the co-electrolysis of H_2O/CO_2 in solid oxide cells powered by renewable electricity. An application of this technology, however, is still challenging because the Ni-based cermet fuel electrodes are susceptible to degradation under redox and coking conditions, requiring protective hydrogen atmosphere to maintain stable operation. Perovskite oxides are the most promising alternatives due to their redox stability, extensive range of functionalities and the exsolution concept. The latter allows perovskites to be decorated with uniformly dispersed Ni nanoparticles with unique functionalities that can dramatically enhance the performance. Herein, we demonstrate the advantage of employing a nanoparticle-decorated $La_{0.43}Ca_{0.37}Ni_{0.06}Ti_{0.94}O_3$ (LCT-Ni) perovskite to efficiently generate syngas at adjustable H_2/CO ratios and simultaneously avoid the need of a reducing agent, hence decreasing the total cost and complexity of the process.

1. Introduction

Over the past decades, hydrogen has gained great interest as a potential energy carrier due to limited fossil fuel resources and environmental considerations [1]. Nonetheless, a possible transformation of the existing liquid hydrocarbon infrastructure to a hydrogen-based one is still far from being economically viable [2,3]. The use of renewable energy for the production of synthetic fuels might be an efficient solution for a sustainable future, since the investments required to modify the existing infrastructure are avoided and carbon dioxide emissions could be stabilized [2,3].

The key-intermediate for synthetic fuels, syngas (H_2 + CO), is mainly derived from natural gas reforming and coal gasification processes; both are responsible for significant energy consumption and green-house gases emissions [4]. The co-electrolysis of carbon dioxide and steam in solid oxide electrolysis cells (SOECs) constitutes an emerging route for clean generation of syngas and hence, storing the intermittent renewable electricity in the form of chemical bonds [2,5–11]:
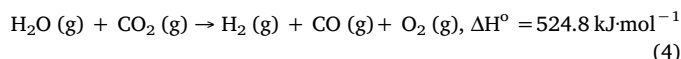
Cathode

$$H_2O \text{ (g)} + 2e^- \rightarrow H_2 \text{ (g)} + O^{2-} \tag{1}$$

$$CO_2 \text{ (g)} + 2e^- \rightarrow CO \text{ (g)} + O^{2-} \tag{2}$$

Anode

$$2O^{2-} \rightarrow O_2 \text{ (g)} + 4e^- \tag{3}$$

Overall reaction

$$H_2O \text{ (g)} + CO_2 \text{ (g)} \rightarrow H_2 \text{ (g)} + CO \text{ (g)} + O_2 \text{ (g)}, \Delta H^o = 524.8 \text{ kJ·mol}^{-1} \tag{4}$$

One can realize that syngas could be also produced by mixing the products of separate carbon dioxide and steam electrolysis processes. A co-electrolysis process, however, is preferable since carbon dioxide splitting is more challenging, and thus results in poor energy efficiencies due to high polarization resistance. Moreover, the absence of steam in dry carbon dioxide electrolysis favor coke formation, which in turn leads to complete deactivation of the electro-catalyst [2,7,8].

The co-electrolysis of steam and carbon dioxide to syngas in a SOEC (Fig.1) constitutes a more complicated process than the two separate electrolysis reactions. At elevated temperatures, the composition of the product stream on the fuel side is dictated by the equilibrium of the reverse water-gas shift reaction (RWGS, $\Delta G = 0$ at $T \approx 815\,°C$) [2,5–12],
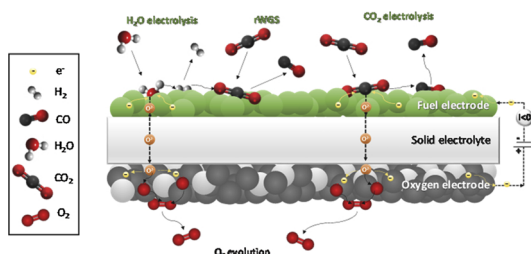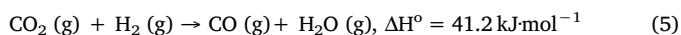
Fig. 1. Schematic illustrating possible processes occurring during high temperature carbon dioxide and steam co-electrolysis in a SOEC.

$$CO_2 \text{ (g)} + H_2 \text{ (g)} \rightarrow CO \text{ (g)} + H_2O \text{ (g)}, \Delta H^o = 41.2 \text{ kJ·mol}^{-1} \qquad (5)$$

Stoots et al. [12] were the first to focus on the reaction mechanism by employing a Ni/yttria-stabilized zirconia (YSZ) cermet as the fuel electrode (cathode) of the cell. It was suggested that only steam electrolysis and RWGS took place in the process (H_2 from steam electrolysis reduced CO_2 to CO). This conclusion was drawn after observing similar area specific resistance (ASR) for H_2O and CO_2/H_2O electrolysis, whereas ASR for CO_2 electrolysis was significantly higher [12]. However, in a more recent study, Ebbesen et al. [3] performed comprehensive AC and DC characterization, which suggested that both CO_2 electrolysis as well as oxidation of CO and H_2 took place in the SOEC. The higher overpotential for CO_2 electrolysis than co-electrolysis of CO_2-H_2O was partly attributed to impurities (possibly sulfurous gases), which had larger impact on the reaction rate of CO_2 electrolysis [3]. Today, the direct electroreduction of CO_2 is considered possible, but less favorable than the RWGS route, particularly under low applied bias [2,5,13–16].

In SOECs, Ni/YSZ cermets are most commonly employed as fuel electrode, due to their high ionic and electronic conductivity, as well as electro-catalytic activity for H_2O/CO_2 splitting [2,5,12–19]. Nevertheless, Ni-based cermet electrodes have significant drawbacks, which include sensitivity to microstructure changes caused under redox conditions and susceptibility to impurities such as sulfur (typically present in the feed stream) and coking even under high steam concentrations [5,20–22]. Among them, the redox instability of Ni/YSZ is the most significant disadvantage, considering that SOEC cathodes are exposed to a wide range of oxygen partial pressures. To avoid oxidation of Ni, small concentrations of protecting hydrogen are usually introduced in the cathode atmosphere, thus increasing the cost and complexity of the process [2,4].

Perovskite oxide ceramics (ABO_3) are among the most promising alternative fuel electrodes [2,23]. Perovskites exhibit mixed ionic-electronic conductivity as single phases and can accommodate several kind of defects under redox conditions, allowing them to adapt to various external conditions and therefore maintain stability and functionality under redox environments [23–45]. Additionally, various transition metal cations with high (electro-) catalytic activity may be incorporated at the B-site. Up to date, $(La_{0.75}Sr_{0.25})_{0.97}Cr_{0.5}Mn_{0.5}O_{3-a}$ (LSCM) [23–28] and $Sr_2Fe_{1.5}Mo_{0.5}O_6$ (SFM) [29,43] have shown the most promising results for co-electrolysis process with ASR comparable or even better to the typical Ni-cermet cells. Another important advantage of the above materials is that they can be used as both cathode and anode, hence eliminating the need for a reducing agent (usually hydrogen) at the fuel side and decreasing the overall cell preparation cost [25,26].

Lanthanum titanates constitute an intriguing class of perovskites, exhibiting chemical, dimensional, thermal and mechanical stability. These materials have been successfully applied to high temperature electrochemical processes, as either anodes or cathodes in SOFCs or SOECs, respectively [31–37]. By controlling deficiency of the A-site, transition metal nanoparticles may be exsolved to the surface from the perovskite oxide backbone under reducing environments, i.e. H_2-rich gas phase [33,34] or after imposition of high cathodic overpotentials [35].

The grown particles are uniformly dispersed as well as anchored to the perovskite scaffold, which render them more active and stable against coarsening and coking compared to the oxide supported counterparts prepared by infiltration [32,34–36]. The outstanding performance of such electrodes have been applied successfully to the separate steam [30,32,35] or carbon dioxide [37] high temperature electrolysis processes.

Along these lines, here we explore the performance of such nanostructured perovskites for the direct generation of syngas from the combined electrolysis of CO_2/H_2O in an SOEC. The perovskite examined is $La_{0.43}Ca_{037}Ni_{0.06}Ti_{0.94}O_3$ (LCT-Ni) assembled in a scandia-ceria stabilized zirconia (ScCeSZ) electrolyte-supported cell with a lanthanum strontium manganite (LSM)/YSZ composite oxygen electrode (anode). The socketed Ni nanospheres, exsolved after reduction in hydrogen, are expected to interact strongly with the perovskite scaffold, enhancing not only the electrocatalytic properties, but also the segregation and coking resistivity of the cathode. LCT-Ni performance is benchmarked against a state-of-the-art Ni/YSZ cermet deposited on an identical half-cell. The two SOECs are tested for separate and combined H_2O/CO_2 electrolysis processes as well as in presence and absence of hydrogen reducing agent in order to allow the control of H_2/CO ratio with current.

2. Experimental

2.1. LCT-Ni preparation and cell fabrication

The LCT-Ni ($La_{0.43}Ca_{037}Ni_{0.06}Ti_{0.94}O_3$) oxide was fabricated by a modified solid state synthesis method as described previously [35]. In brief, stoichiometric amounts of high purity La_2O_3 (99.99%, Sigma Aldrich), $CaCO_3$ (99.995%, Alfa Aesar), TiO_2 (99.99%, Sigma Aldrich) and $Ni(NO_3)_3 \cdot 9H_2O$ (99.99%, Sigma Aldrich) precursors were mixed with acetone and a small amount of a non-aqueous dispersant (Hypermer KD-1). The homogenized mixture was dried slowly and calcined at 1000 °C for 12 h in order to decompose the carbonates and start the nucleation of the perovskite. The powder was ball milled in acetone, pressed into dense pellets and fired at 1400 °C for 14 h to achieve the perovskite phase. To investigate the contribution of Ni nanoparticles to the overall electrocatalytic performance of the perovskite, an undoped $La_{0.4}Ca_{0.4}TiO_3$ (LCT) perovskite was also fabricated following the same experimental procedure as described above.

To prepare the electrode precursor, the pellets were crushed and ball-milled at 400 rpm for 2 h. The cells used in this work were based on ScCeSZ solid electrolyte membrane (20 mm diameter, ~0.15 mm thickness, Fuel Cell Materials). Prior to the deposition of the cathode, an adhesion layer (2 mg·cm^{-2}) of gadolinia-doped ceria (GDC) was printed on the one side of the ScCeSZ electrolyte to increase the surface roughness and to bridge the thermal and chemical mismatch of the materials. To prepare the two cathode inks, either the LCT-Ni or the commercial NiO/YSZ (60 wt.%NiO, FC Materials) powders was mixed to a terpineol-based ink vehicle. The viscous suspension was screen-printed on the top of the GDC layer for LCT-Ni (4 mg·cm^{-2}) and Ni/YSZ (6 mg·cm^{-2}). The adhesion layer-cathode-membrane assembly was fired for 4 h at 1250 °C and 1380 °C for LCT-Ni and NiO/YSZ, respectively. The anodic electrode was printed on the opposite side of the electrolyte and constituted of two layers. The layer (5 mg·cm^{-2}) interfacing with the solid electrolyte was a composite strontium doped lanthanum manganite (LSM) and YSZ (FC Materials) at 50-50 wt.% whereas a subsequent pure LSM layer (5 mg·cm^{-2}) was added. The printed layers were fired at 1100 °C for 2 h. The heating and cooling rate in all cases was kept at 80 °C/h. Au paste was painted on the electrodes and sintered at 850 °C for 2 h to improve current collection. The effective electrode area was approximately 0.40 cm^2.

The electrochemical studies were carried out under atmospheric pressure in a dual-chamber configuration consisting of a quartz tube, closed at one end and an alumina tube, open at both ends. These tubes,

forming the outer and the inner chamber of the reactor cell, respectively, are connected to a stainless steel "reactor head", which ensures gas tightness through high temperature o-ring Ultra-Torr junctions (Swagelok). It also separates inlets and outlets of both chambers and provides electrical connections by means of Au wires. To seal the cell sample to the ceramic tube, an alumina-based cement (Cotronics) was applied.

2.2. Characterization and testing

The phase purity and crystal structure of the perovskite was examined by room temperature XRD with a Bruker instrument using nickel-filtered Cu Kα beam operating at 40 kV, 40 mA and a scan rate of 0.02° in the 2θ range of 20°-90°. Structural analysis by Rietveld refinement was carried out using GSAS II software package The microstructure of the cells was characterized by scanning electron microscopy (SEM) with a SEM Quanta 3DFEG600. The instrument was also equipped with an energy dispersive X-ray spectroscopy (EDX) analyzer to determine the average composition of the samples. Chemical analysis of the samples was carried out by X-ray photoelectron spectroscopy (XPS) using a Thermo Fisher Scientific, K-alpha instrument. The elemental composition of the surfaces was studied in vacuum ($1 \cdot 10^{-8}$ mbar) with monochromatic Al-Ka radiation. Quantification was performed using sensitivity factors from the Scofield library based on the area of peaks of interest (Ca 2p, La 3d, Ti 2p) after the subtraction of background of appropriate shape.

The imposition of constant current or voltage and impedance spectroscopy were performed by using an electrochemical station (CompactStat, Ivium Technologies B.V.). The current-voltage (I–V) curves were recorded with a voltage sweeping speed of 20 mV·s^{-1}. Electrochemical impedance spectra (EIS) under both the OCV and

electrolysis conditions were evaluated under the voltage amplitude of 20 mV at frequencies between 4×10^5 and 0.01 Hz. The electrochemical experiments were carried out at an operation temperature of 850 °C with total flowrates between 50 and 100 sccm to operate at low conversion (< 5%) and differential mode. The CO_2, air, H_2 and N_2 gases were certified standards of 99.999% purity (Air Liquide) and their flows were controlled by means of mass flow controllers (Brooks). Water vapor was added by bubbling cathode gas stream through a temperature controlled saturator. The pipes from the saturator to the furnace were heated above 120 °C to avoid water condensation. Finally, the analysis of the effluents was performed by using an on-line microGas Chromatograph (SRA instruments) and an infra-red analyzer (Fuji Electric).

3. Results and discussion

3.1. Solid oxide cell structure and microstructure

The phase purity and crystal structure of the LCT-Ni material was analyzed by Rietveld refinement. At room temperature the material exhibits a single phase, Ibmm type structure (see Fig. 2a), depicting out of phase tilting described by $a^0b^-b^-$ in the Glazer tilt notation. The SEM images in Fig. 2b and c display the morphology of a fractured LCT-Ni sample, before and after thermal reduction. The sample was fractured to reveal the difference in particle exolution between native surfaces and freshly cleaved surfaces. It has been shown previously that during sintering or thermal treatments perovskite develop a different structure and composition which is generally A-site rich and usually referred to as "native surface" [33]. This usually limits exolution kinetically, acting as a release barrier for the particles exolution. Thus, the exolution on native surface is indicative of particle populations that may be achieved in regular electrode microstructures after the initial
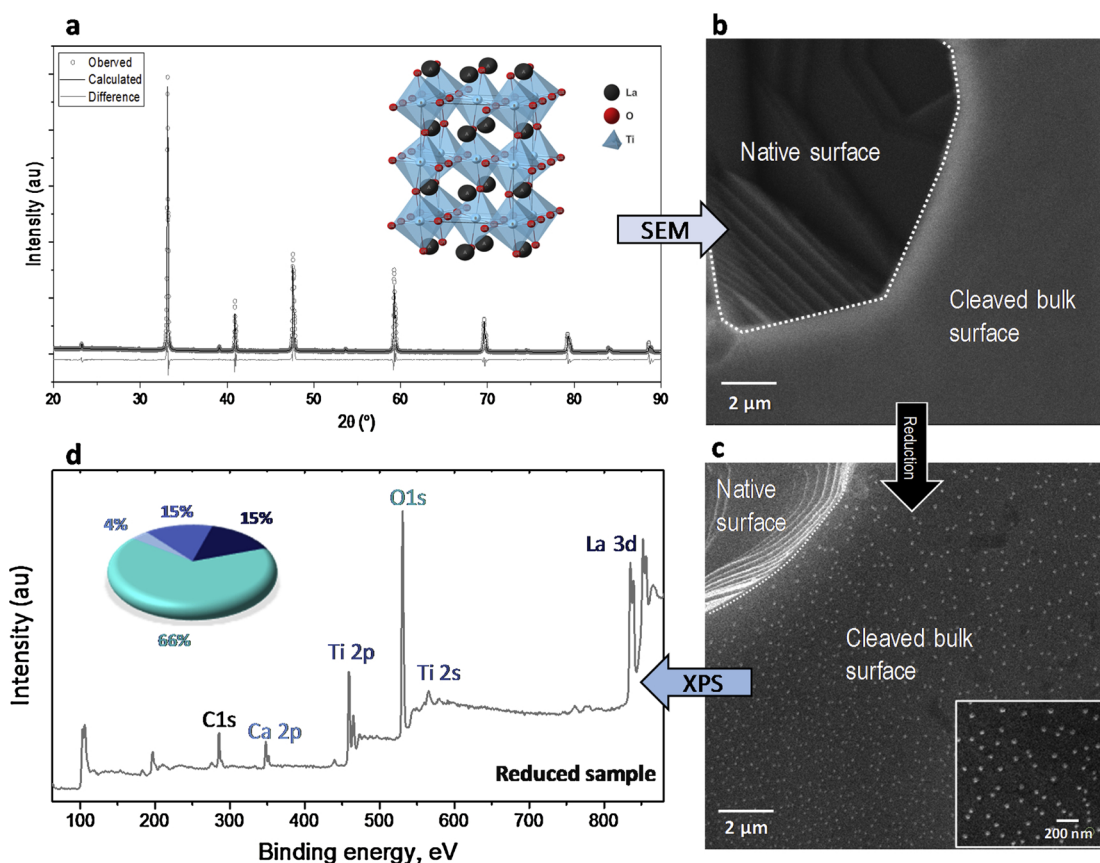

Fig. 2. Crystallographic, microstructure and surface analysis of LCT-Ni. **a.** Rietveld Refinement analysis and corresponding crystal structure (Ibmm, a = 5.4741 Å, b = 5.4650 Å, c = 7.7188 Å). SEM images of the **b.** as-prepared and **c.** reduced LCT-Ni perovskite. **d.** Surface analysis and quantification pie chart of the reduced sample by XPS.
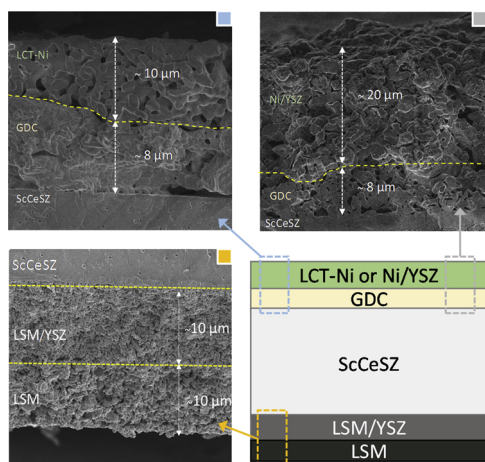
Fig. 3. Structure and the corresponding cross-section SEM images of LCT-Ni and NiO/YSZ as-fabricated cells.

reduction, while the cleaved regions are illustrative of potential exolution population that can be achieved after long-term operation, if the surface blocking effects can be overcome, e.g. *via* strong electrochemical reduction [35].

As expected, no Ni nanoparticles were observed on the surfaces of LCT-Ni before the reduction procedure. Upon exposure to 10% H_2/N_2 at 900 °C for 10 h, uniformly exsolved on the surface of the perovskite. The population of the nanoparticles was 50–60 particles per square micron and existed within a diameter size distribution of 35–45 nm with an average of 40 nm. The quantitative analysis from the XPS survey of the reduced sample showed that the atomic ratio between La/Ca/Ti was 1.01/0.27/1. This is consistent with a perovskite surface that is expected to be slightly A-site and La-rich after the exsolution process.

Fig. 3 depicts the cross-section microstructure of LCT-Ni and NiO/YSZ//GDC//ScCeSZ//LSM/YSZ//LSM fabricated cells. The cell composites were verified by EDX analysis and the dashed lines were manually added to distinct the various interfaces of the cells. The LCT-Ni electrode thickness was close to 10 μm and with relatively low porosity. The low thickness of LCT-Ni was necessary to decrease the ohmic losses of the electrode since its electronic conductivity is modest (~ 15 S·cm^{-1} after reduction). On the other hand, the NiO/YSZ electrode was around 20 μm thick with a quite dense structure. The necessary open porosity of the electrode is achieved after the thermal reduction of NiO to metallic Ni by hydrogen. A thin and dense GDC layer was deposited between the fuel electrode and the electrolyte in order to improve the adhesion of the fuel electrode with the electrolyte. The GDC layer was well attached to both the fuel electrode and the ScCeSZ ceramic electrolyte after sintering at 1300 °C for 4 h. Regarding the oxygen electrode, the double-layered LSM/YSZ//LSM exhibits good adhesion to the electrolyte, high open porosity to facilitate gas diffusion and uniform size distribution.

After fabrication, the cells were mounted in the testing setup and the cathodes were reduced with H_2 at 900 °C. The LCT-Ni was reduced by introducing 5%H_2 for 10 h, whereas Ni/YSZ by a 25–100% H_2 varying concentration with steps of 25%, each one of 30 min duration. The XRD analysis of LCT-Ni electrode prior and after the reduction stage revealed that the characteristic peak of metallic Ni (111) at 44.4° appeared only after the reduction stage, verifying the existence of Ni on the surface (Fig.4a). Moreover, Fig. 4b displays back-scattered electron (BSE) images of the electrode surface, where uniformly decorated Ni particles (35–45 nm) are seen across the electrode as bright spots.

3.2. Electrochemical performance

Following the reduction stage, the operation temperature was set at 850 °C for the electrochemical experiments. The balance of the gas mixture was in all studies N_2, whilst air was always supplied to the anode in all
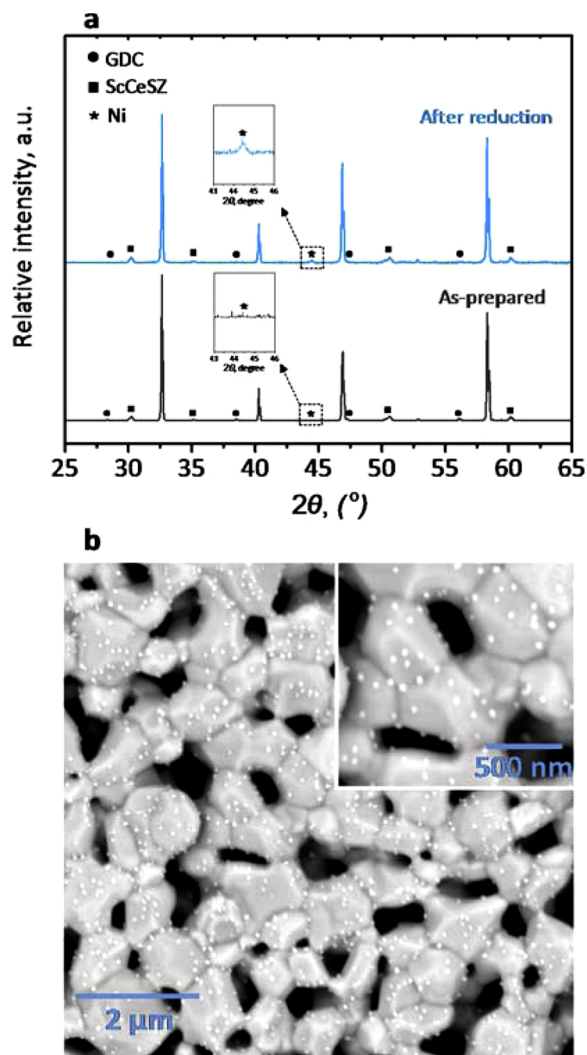

Fig. 4. a. Room temperature XRD of the LCT-Ni electrode prior and after the reduction process. **b.** Back-scattered electron (BSE) image of the reduced electrode surface with the Ni exsolved nanoparticles (bright spots) to be uniformly decorated across the perovskite surface.

experiments. For simplicity, only the gas composition at the cathode side will be stated below. Gas-tightness of the cell was verified with a pure hydrogen feed at the cathode of the cell reactor. An OCV of ~1.1 V was observed with all tested cells, implying adequate separation between the two chambers. The electrocatalytic performance of LCT-Ni and Ni/YSZ was evaluated under reversible fuel/electrolysis cell operation. The feed gas concentrations at the cathode were: a) 25% H_2O - 50% H_2, b) 25% H_2O - 25% CO_2 - 50% H_2 and c) 25% CO_2 - 50% H_2 with a total volumetric flowrate of 100 sccm. The electrochemical performance of the two cells is compared in Fig. 5 through Nyquist plots and characteristic current-voltage curves. The EIS data were recorded under open-circuit voltage (OCV) conditions in order to obtain information for both H_2 and/or CO (produced via the RWGS) oxidation, as well as H_2O-CO_2 electrolysis reactions. In all cases, two main arcs were observed. LCT-Ni displays significantly lower polarization resistance (Rp) than Ni/YSZ under all gas compositions examined. Specifically, Rp of LCT-Ni was 0.50, 0.49 and 0.52 Ω·cm^2 for H_2O, H_2O-CO_2 and CO_2, respectively, whereas the corresponding of Ni/YSZ were 0.69, 0.69 and 0.71 Ω·cm^2. The detailed results of the EIS analysis are presented in Table S1.
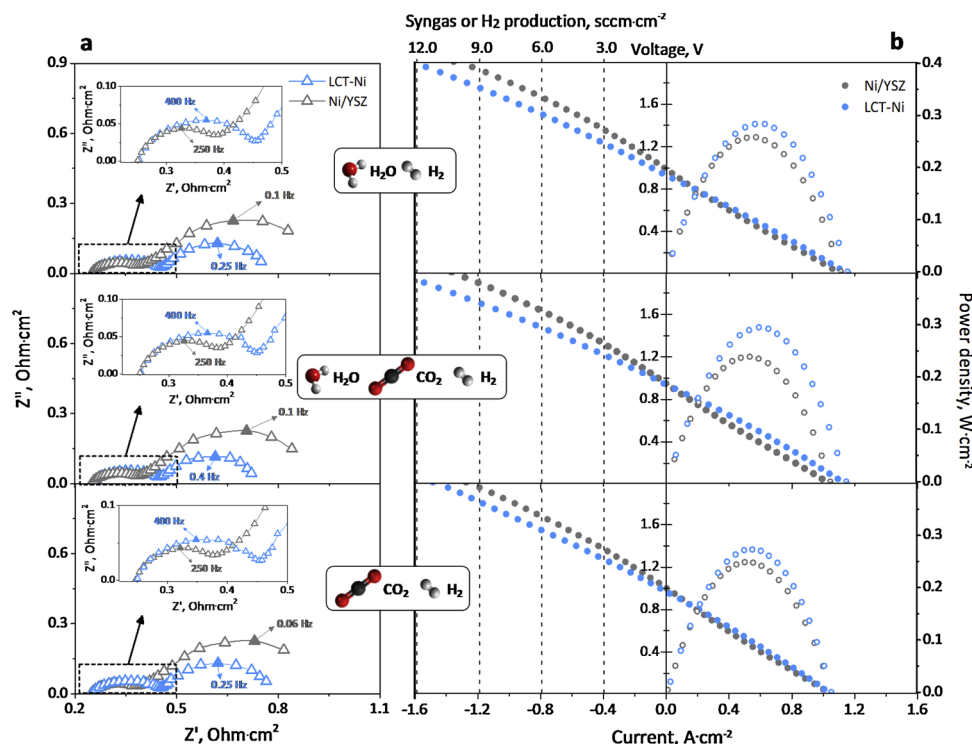
Fig. 5. Electrochemical performance of LCT-Ni and Ni/YSZ cells under reversible SOC operation at 850 °C. **a.** Nyquist plots and **b.** I–V polarization curves for H_2O (25% H_2O - 50% H_2 - 25% N_2), H_2O-CO_2 (25% H_2O - 25% CO_2 - 50% H_2) and CO_2 (25% CO_2 - 50% H_2 - 25% N_2) feed.

Fig. 5b shows the characteristic I–V curves under the same gas compositions as in the AC analysis, while keeping the scan rate of $20\,mV \cdot s^{-1}$. The negative current densities indicate electrical power consumption (SOEC mode), whereas the positive indicate power generation (SOFC mode). In the SOFC region of the graphs the power output is plotted, whilst at the SOEC side, we have added the hydrogen or syngas production rate, which corresponds to the applied current density. The I–V curves transit smoothly between the two operation modes, following an almost linear trend, implying very good reversibility between the two operation modes. By employing LCT-Ni perovskite instead of Ni/YSZ the current density of the cell increased up to 20% under electrolysis conditions and it exceeded 1.6 $A \cdot cm^{-2}$ (12.0 $sccm \cdot cm^{-2}$ of syngas) at 2.0 V. On the other hand, in SOFC mode, the power densities were rather moderate and reached up to 0.3 W cm^{-2} but were always higher than of Ni/YSZ analogue cells under the same conditions.

At electrolysis operation and under similar gas concentrations current densities ~ 1.0 $A \cdot cm^{-2}$ upon application of 1.3–1.4 V have been reported for Ni/YSZ [3–6,13,46]. In the present Ni/YSZ cell, the current density did not exceed 0.45 $A \cdot cm^{-2}$ at CO_2-H_2O co-electrolysis operation. Nonetheless, the impressive current densities in literature were always achieved with electrode-supported electrolytes of less than $10\,\mu m$ thickness, whereas the ScCeSZ used here had a thickness of $150\,\mu m$. If the present results are compared to electrolyte-supported Ni/

YSZ cells [17,18,25], the observed values are slightly higher demonstrating the adequate activity of our cell.

Table 1 summarizes the observed and thermodynamically calculated OCVs, together with the ASR values derived from the I–V curves of Fig. 4b for LCT-Ni and Ni/YSZ cells. The observed OCVs ranged from 0.956-0.990 V, consistent, albeit slightly below, the thermodynamically predicted ones (0.962-0.995) implying a small gas or electronic leak during the experimental testing. From each I–V curve, two ASRs are derived, one for electrolysis and one for fuel cell mode. The ASR was determined as the difference between the cell voltage corresponding to 0.2 (-0.2 for electrolysis) $A \cdot cm^{-2}$ and OCV divided by the current density of 0.2 $A \cdot cm^{-2}$. The fuel cell ASR provides information for H_2 and/or CO oxidation (produced via the RWGS) to H_2O and/or CO_2, whilst the electrolysis ASR for the reverse reactions. The measured values are slightly higher for CO_2 electrolysis than for H_2O and H_2O-CO_2 electrolysis processes for both electrodes. The lowest ASR of 0.73 $\Omega \cdot cm^{-2}$ was obtained under co-electrolysis of 25% H_2O - 25% CO_2 conditions by employing LCT-Ni perovskite as cathode and it was by 0.2 Ω lower than N/YSZ at the same conditions.

The lower ASR of LCT-Ni is attributed to the combination of two factors. The first is the intrinsic electrocatalytic activity of the host LCT perovskite at reducing conditions as seen in Fig. S3. The second is that LCT's performance is enhanced by more than two times when uniformly

Table 1
Open-circuit voltage (OCV) and area specific resistance for the various gas compositions on LCT-Ni and Ni/YSZ electrodes as extracted from Fig. 4.

Fuel electrode	Gas composition on the cathode	Open-circuit voltage (V)		Area specific resistance ($\Omega \cdot cm^2$)	
		Experimental	Theoretical	Electrolysis	Fuel cell
LCT-Ni	25% H_2O - 50% H_2 - 25% N_2	0.981	0.996	0.74	0.75
	25% H_2O - 25% CO_2- 50% H_2	0.956	0.962	0.73	0.74
	25% CO_2 - 50% H_2 - 25% N_2	0.984	0.995	0.76	0.77
Ni/YSZ	25% H_2O - 50% H_2 - 25% N_2	0.989	0.996	0.93	0.94
	25% H_2O - 25% CO_2 - 50% H_2	0.956	0.962	0.93	0.94
	25% CO_2 - 50% H_2 - 25% N_2	0.990	0.995	0.95	0.94

Fig. 6. Cell voltage transients during galvanostatic electrolysis of **a.** 25% H_2O, **b.** 25% H_2O - 25% CO_2 and **c.** 25% CO_2 with 10% H_2 on (white areas) and off cycles (grey areas).

distributed Ni nanospheres grow on its surface, thus increasing the catalytic surface area of the perovskite. Moreover, in exsolution the Ni particles are partly submerged in the perovskite oxide backbone leading to enhanced metal-support interactions that are well-connected to increased catalytic activity.

3.3. Impact of H_2 protective atmosphere on cathode stability

To assess the role of protective H_2 in the stability of LCT-Ni and Ni/YSZ cells, transient electrolysis experiments with consecutive H_2 co-feed on-off cycles were conducted. Fig. 6 displays the measured voltage of both cells during electrolysis of a) 25% H_2O, b) 25% H_2O - 25% CO_2 and c) 25% CO_2 with 10% H_2. Initially, 10% of hydrogen was supplied to the cells for at least 1 h and the electrolysis voltage was stabilized. The LCT-Ni demanded less applied potential (and thus less electrical energy) than Ni/YSZ to produce the same amount of syngas. When the H_2 feed was interrupted, the voltage slightly increased under all examined mixtures. A similar picture of the cell voltage was obtained during the second on-off hydrogen cycle. Although, the difference between LCT-Ni and Ni/YSZ samples grew even larger since the latter exhibited some slight degradation even during the small cycle time periods. LCT-Ni behavior was almost unaltered by the H_2 cycles under steam and co-electrolysis conditions, in which a steady-state was always significantly increased for both electro-catalysts, indicating slower kinetics of the CO_2 than H_2O electrolysis. This finding is in good agreement with previous works conducted under similar gas environments and cell components, where also H_2O electrolysis was favoured under low applied bias (< 1.4 V) [3].
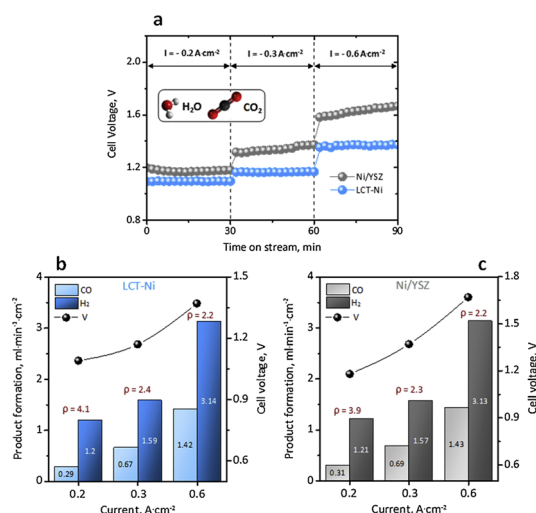

Fig. 7. a. Effect of time on stream on the cell voltages of LCT-Ni and Ni/YSZ under 0.20, 0.30 and 0.60 A· cm^{-2} and **b. c.** the corresponding syngas production rates as well as H_2/CO ratio (ρ) during the 25% H_2O - 25% CO_2 co-electrolysis experiment.

3.4. Evaluation of syngas production

The syngas production in the cell was determined by performing transient experiments under co-electrolysis conditions. These studies were carried out under 25% H_2O - 25% CO_2 without co-feeding H_2 as protective atmosphere at various applied currents (0.2-0.6 A·cm^{-2}) and the results are illustrated in Fig. 7. Galvanostatic operation was selected since a constant removal of O^{2-} from the fuel electrode, corresponds to a set formation rate of syngas (CO_2 + H_2O + $2e^-$ → CO + H_2 + $2O^{2-}$) if the faradaic efficiency approaches 100%. The latter was also verified in the present studies by monitoring the products *via* online gas-chromatography. A steady state under open-circuit conditions was firstly achieved (15–20 min) and subsequently, currents of 0.20, 0.30 and 0.60 A·cm^{-2} were applied, developing cell voltages of 1.09–1.37 V and 1.18–1.67 V for LCT-Ni and Ni/YSZ cathodes, respectively. The cell voltage was constant during the 30 min steps at all currents examined with LCT-Ni perovskite as the fuel electrode. Although, Ni/YSZ exhibits a small degradation under these conditions (i.e. absence of hydrogen protection, especially at 0.30 and 0.60 A·cm^{-2} applied currents. Figs. 7b-c depict the formation rate of H_2 and CO at the two fuel electrodes under three different currents. In all cases, hydrogen again constituted the main product denoting the dominance of the H_2O electrolysis process. Specifically, H_2 formation reached up to 3.14 sccm·cm^{-2} at 0.60 A·cm^{-2}, while the corresponding of CO was 1.43 sccm·cm^{-2} under the same conditions.

The mechanism of syngas production at the fuel electrode of the co-electrolysis cell is rather complex, since CO may be formed by both CO_2 electrolysis at the active electrochemical zone (three-phase boundary) as well as the reverse water-gas shift reaction (eq. 5) on the whole surface of the fuel electrode [2,3,5–12]. The contribution for each path to CO formation is still debatable and quite sensitive to the operation conditions (temperature, gas composition, flowrate, materials etc.) of the cell [2,3,5–12]. Our results in Figs. 6 and 7 suggests that both pathways occur over LCT-Ni and Ni/YSZ. As seen in Fig. 6, the existence of H_2 and H_2O leads to lower operation voltages compared to dry CO_2 electrolysis, indicating that the latter is not kinetically favoured in our systems compared to H_2O electrolysis. The slower CO_2 electrolysis kinetics indicate that the main pathway for CO generation at the lower applied currents (< 0.3 A·cm^{-2}) was the catalytic RWGS reaction, whereas as current and voltage increased, the contribution from CO_2 electrolysis became significant.

This conclusion can also be supported by the decline in H_2/CO ratio

(ρ) by raising the applied current. This ratio constitutes an essential parameter to characterize the synthesis gas process and its possible industrial application [47]. Most chemical industries use syngas of ρ between 1.0 and 3.0 as their raw material [47]. Here, by avoiding H_2 co-feed, we accurately measured this parameter under various imposed currents. The observed ρ were almost similar for both Ni/YSZ and LCT-Ni and ranged from 2.2-4.1. The ρ control by the applied current (or voltage) reveals another important advantage of the electrochemical syngas production (Fig. 7b-c), since depending on the industrial application the current-voltage could be adjusted accordingly.

3.5. Durability test

To evaluate the durability of LCT-Ni and Ni-/YSZ cells, a constant current of 0.60 A·cm^{-2} was imposed under 25% H_2O - 25% CO_2 co-electrolysis conditions and the voltage was recorded for 48 h as a function of time (Fig. 8a). The Ni/YSZ cell showed rapid degradation with a voltage increase of ~0.5 V (from 1.54 to 2.03 V) during the testing period. The morphological analysis of the used Ni/YSZ revealed major delamination of Ni particles from the cermet structure due to coarsening (Fig. 8b). On the other hand, LCT-Ni cell performance was practically unaltered (from 1.37 to 1.39 V after 48 h) under the same conditions, demonstrating the exceptional behavior of the Ni-exsolved perovskite for co-electrolysis. The marginal increase of the voltage was mainly attributed to current collection issues (partial contact loss between Au mesh and electrodes) occurring due to high operation temperature.

In cermet electrodes, Ni has supporting, current collective, as well as catalytic role. In the absence of a reducing agent Ni is converted to NiO, thus leading to the deterioration of cermet's structure and consequently to its irreversible deactivation. In the LCT-Ni architecture, however, Ni keeps only its catalytic role because the particles are isolated (i.e. not percolating), whereas the perovskite fulfils the rest of functions. Moreover, another reason of cermet's degradation is the poor electric conductivity of NiO compared to metallic Ni. This is not an issue in LCT-Ni since the current collection role is played by the perovskite backbone. Regarding the catalytic role, when Ni is oxidized it loses a major part of its catalytic activity. Though, this could occur in both type of electrodes, the small size and anchored nature of Ni nanoparticles render them redox stable, and an electrochemical reduction occurs by electrons flowing through the perovskite backbone's lattice.

The microstructure changes of LCT-Ni after the 48-h durability study were examined by performing SEM at the electrode's cross-section (Fig. 8c). On the surface close to the GDC adhesion layer, which actually was the active electrochemical zone of the electrode (extends 5 μm above GDC), Ni NPs population was about 150 particles/micron^2, increased by almost three times from the freshly reduced sample (40–50 particles/micron^2, Fig.S2). The imposition of a negative current (cathodic polarization) results in an electron flooding on the surface, which in turn favors Ni nucleation and the formation of numerous new particles, thus enhancing the electro-catalytic activity and stability of the fuel electrode [35,36]. However, on moving away from the active electrochemical zone, Ni particle population was observed to decline to
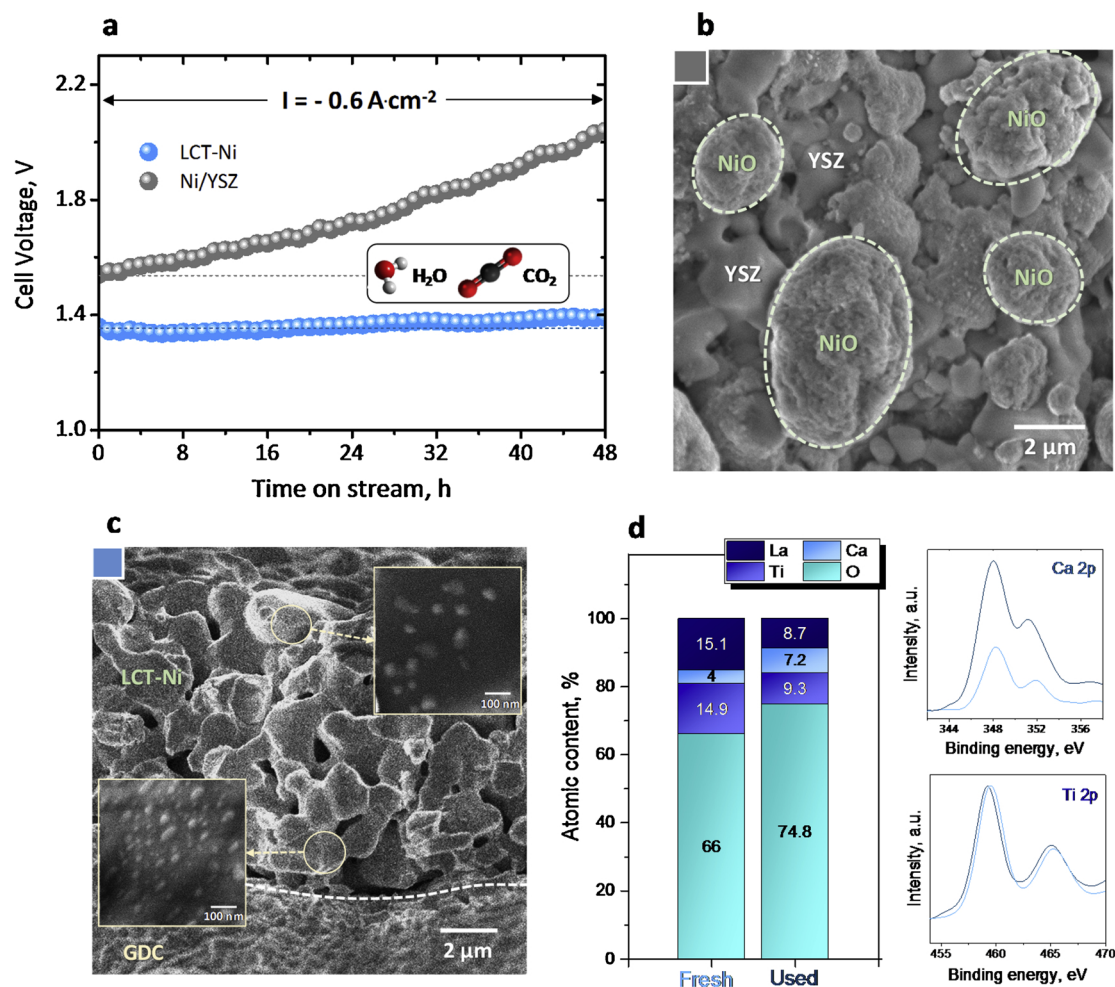

Fig. 8. a. Durability study of LCT-Ni and Ni/YSZ cells during the 48-h co-electrolysis experiment in absence of hydrogen protection. Reaction conditions: 25% H_2O - 25% CO_2 - 50% N_2, I = 0.60 A·cm^{-2}, F_t =100 sccm. SEM micrographs of **b.** Ni/YSZ top surface and **c.** LCT-Ni cross-section after the stability test. **d.** Quantification by XPS of LCT-Ni surface before and after the stability test.

values similar to the ones observed at the fresh sample.

The elemental quantification *via* XPS on the top surface of LCT-Ni electrode revealed an enhancement of Ca atomic concentration after the stability test (Fig.8d). The segregation of an A-site cation (such as Ca) on the perovskite surface hinders exsolution and is usually observed under high oxygen partial pressures [39,48]. This is due to the fact that under oxidizing atmospheres, the oxidation state of the transition B-site metals increases and its ionic radius decreases, thus increasing ionic size mismatch as compared to the A-site, which in turn favors A-site-cation segregation towards the surface [39,48]. The above findings from SEM and XPS analysis indicate a strong variation of the environment across the LCT-Ni fuel electrode. Close to GDC layer ($< 5 \mu m$), where the electrochemical zone is located, strongly reducing conditions dominate, caused by the high corresponding potential applied. Further from this area (5–10 μm from GDC), however, H_2 or CO produced by the electrolysis processes were not of sufficient concentration to maintain a sufficiently low P_{O_2} and therefore the perovskite was oxidized by the high CO_2 and steam concentrations in the gas-phase. The higher oxygen content of the used sample usually reflects an increased surface area due to the formation of nanoparticles consistent with our SEM observations.

4. Conclusions

A $La_{0.43}Ca_{0.37}Ni_{0.06}Ti_{0.94}O_3$ perovskite cathode decorated with Ni exsolved nanoparticles (35–45 nm) after thermal reduction by H_2 was employed as the fuel electrode of H_2O, CO_2-H_2O and CO_2 electrolysis processes in a ScCeSZ supported cell. As compared to a conventional Ni/YSZ cermet deposited in an identical half-cell, LCT-Ni performance reduced by up to 20% the electricity demands under co-electrolysis of CO_2 and H_2O at 850 °C. Most notably, when a reducing agent was not introduced to the cathode side, Ni particle coarsening lead to an almost complete deterioration of Ni/YSZ after 48 h. By carrying out the same test, LCT-Ni activity was practically unaffected, while the absence of protective H_2 at the cathode's gas atmosphere allowed an accurate evaluation of imposed current's effect on H_2/CO ratio. The exceptional behavior of LCT-Ni was attributed to the three-fold increase in Ni particle population at the active electrochemical zone due to the reduction by electrons under cathodic polarization. The results obtained here, clearly demonstrate the advantage of employing nanoparticle decorated perovskites to efficiently generate syngas at adjustable H_2/ CO ratios and simultaneously avoid the need of a reducing agent, hence diminishing the total cost and complexity of the process.

Acknowledgements

Appendix A. Supplementary data

Supplementary material related to this article can be found, in the online version, at doi:https://doi.org/10.1016/j.apcatb.2019.117950.

References

[1] J.A. Ritter, A.D. Ebner, Sep. Sci. Technol. 42 (2007) 1123–1193.

[2] Y. Zheng, J. Wang, B. Yu, W. Zhang, J. Chen, J. Qiao, J. Zhang, Chem. Soc. Rev. 46 (2017) 1427–1463.

[3] S.D. Ebbesen, R. Knibbe, M. Mogensen, J. Electrochem. Soc. 159 (2012) F482–F489.

[4] B. Sørensen, Hydrogen and Fuel Cells: Emerging Technologies and Applications, second ed., Elsevier, Burlington, 2005.

[5] C. Graves, S.D. Ebbesen, S.H. Jensen, S.B. Simonsen, M.B. Mogensen, Nat. Mat. 14 (2015) 239–244.

[6] S.R. Foit, I.C. Vinke, L.G.J. de Haart, R.A. Eichel, Angew. Chem. Int. Ed. Engl. 56 (20) (2017) 5402–5411.

[7] R.I. Masel, Z. Liu, D. Zhao, Q. Chen, D. Lutz, L. Nereng, CO_2 conversion to chemicals with emphasis on using renewable Energy/Resources to drive the conversion, in: S.W. Snyder (Ed.), Commercializing Biobased Products: Opportunities, Challenges, Benefits, and Risks, Royal Society of Chemistry, Cambridge, 2016, pp. 215–257.

[8] C. Graves, S.D. Ebbesen, M. Mogensen, K.S. Lackner, Renew. Sust. Energ. Rev. 15 (2011) 1–23.

[9] A. Goeppert, M. Czaun, J.P. Jones, G.K. Surya Prakash, G.A. Olah, Chem. Soc. Rev. 43 (2014) 7995–8048.

[10] V.N. Nguyen, L. Blum, Chem. Ing. Tech. 87 (2015) 354–375.

[11] Y. Wang, T. Liu, L. Lei, F. Chen, Fuel Process. Technol. 161 (2017) 248–258.

[12] C.M. Stoots, J.E. O'Brien, J.S. Herring, J.J. Hartvigsen, J. Fuel Cell Sci. Technol. 6 (2009) 011014-1–011014-12.

[13] S.D. Ebbesen, C. Graves, M. Mogensen, Int. J. Green Energy 6 (2009) 646–660.

[14] W.Y. Li, H.J. Wang, Y.X. Shi, N.S. Cai, Int. J. Hydrog. Energy 38 (2013) 11104–11109.

[15] X.B. Chen, C.Z. Guan, G.P. Xiao, X.L. Du, J.Q. Wang, Faraday Discuss. 182 (2015) 341–351.

[16] A. Mahmood, S. Bano, J.H. Yu, K.H. Lee, J. Membrane Sci. 473 (2015) 8–15.

[17] C. Neofytides, M. Athanasiou, S.G. Neophytides, D.K. Niakolas, ECS Trans. 68 (1) (2015) 1353–1360.

[18] D.K. Niakolas, C.S. Neofytidis, S.G. Neophytides, Front. Environ. Sci. 5 (78) (2017) 1–20.

[19] A. Hauch, K. Brodersen, M. Chen, M.B. Mogensen, Solid State Ion. 293 (2016) 27–36.

[20] A. Atkinson, S. Barnett, R.J. Gorte, J.T.S. Irvine, A.J. McEvoy, M. Mogensen, S.C. Singhal, J. Vohs, Nat. Mater. 3 (1) (2004) 17–27.

[21] L. Yang, Z. Cheng, M. Liu, L. Wilson, Synth. Lect. Energy Environ. Technol. Sci. Soc. 3 (11) (2010) 1804–1809.

[22] F. Paloukis, K.M. Papazisi, T. Dintzer, V. Papaefthimiou, V.A. Saveleva, S.P. Balomenou, D. Tsiplakides, F. Bournel, J.J. Gallet, S. Zafeiratos, ACS Appl. Mater. Inter. 9 (30) (2017) 25265–25277.

[23] X. Zhang, Y. Song, G. Wang, X. Bao, J. Energy Chem. 26 (2017) 839–853.

[24] F.M. Sapountzi, S. Brosda, K.M. Papazisi, S.P. Balomenou, D. Tsiplakides, J. Appl. Electrochem. 42 (9) (2012) 727–735.

[25] K.M. Papazisi, D. Tsiplakides, S.P. Balomenou, ECS Trans. 78 (1) (2017) 3197–3204.

[26] X.L. Yue, J.T.S. Irvine, Solid State Ion. 225 (2012) 131–135.

[27] R.M. Xing, Y.R. Wang, Y.Q. Zhu, S.H. Liu, C. Jin, J. Power Sources 274 (2015) 260–264.

[28] M. Torrell, S. Garcia-Rodriguez, A. Morata, G. Penelas, A. Tarancon, Faraday Discuss. 182 (2015) 241–255.

[29] Y. Wang, T. Liu, S.M. Fang, F.L. Chen, J. Power Sources 305 (2016) 240–248.

[30] G. Tsekouras, J.T.S. Irvine, J. Mater. Chem. 21 (2011) 9367–9376.

[31] D. Neagu, J.T.S. Irvine, Chem. Mater. 23 (2011) 1607–1617.

[32] G. Tsekouras, D. Neagu, J.T.S. Irvine, Synth. Lect. Energy Environ. Technol. Sci. Soc. 6 (2013) 256–266.

[33] D. Neagu, G. Tsekouras, D.N. Miller, H. Menard, J.T.S. Irvine, Nat. Chem. 11 (2013) 916–923.

[34] D. Neagu, T.S. Oh, D.N. Miller, H. Menard, S.M. Bukhari, S.F. Gamble, R.J. Gorte, J.M. Vohs, J.T.S. Irvine, Nat. Commun. 6 (2015) 8120.

[35] J.-H. Myung, D. Neagu, D.N. Miller, J.T.S. Irvine, Nature 537 (7621) (2016) 528–531.

[36] J.T.S. Irvine, D. Neagu, M.C. Verbraeken, C. Chatzichristodoulou, C. Graves, M.B. Mogensen, Nat. Energy 1 (2016) 15014.

[37] L. Ye, M. Zhang, P. Huang, G. Guo, M. Hong, C. Li, J.T.S. Irvine, K. Xie, Nat. Comm. 8 (2017) 14785.

[38] K.Y. Lai, A. Manthiram, Chem. Mater. 30 (2018) 2515–2525.

[39] Y. Li, W. Zhang, Y. Zheng, J. Chen, B. Yu, Y. Chen, M. Liu, Chem. Soc. Rev. 46 (2017) 6345–6404.

[40] Y. Wang, T. Liu, M. Li, C. Xia, B. Zhou, F. Chen, J. Mater. Chem. A Mater. Energy Sustain. 4 (2016) 14163–14169.

[41] M. Li, B. Hua, Y. Zeng, B.S. Amirkhiz, J.L. Luo, J. Mater. Chem. A Mater. Energy Sustain. 6 (2018) 15377–15385.

[42] X. Xu, W. Wang, W. Zhou, Z. Shao, Small Methods 2 (2018) 1800071.

[43] L. Lei, Y. Wang, S. Fang, C. Ren, T. Liu, F. Chen, Appl. Energy 173 (2016) 52–58.

[44] J. Lu, C. Zhu, C. Pan, W. Lin, J.P. Lemmon, F. Chen, C. Li, K. Xie, Sci. Adv. 4 (2018) eaar5100.

[45] A. Chrzan, S. Ovtar, P. Jasinski, M. Chen, A. Hauch, J. Power Sources 353 (2017) 67–76.

[46] M. Lo Faro, S.C. Zignani, S. Trocino, V. Antonucci, A.S. Aricò, Electrochim. Acta 296 (2019) 458–464.

[47] Y. Cao, Z. Gao, J. Jin, H. Zhou, M. Cohron, H. Zhao, H. Liu, W. Pan, Energ. Fuels 22 (2008) 1720–1730.

[48] W. Lee, J.W. Han, Y. Chen, Z. Cai, B. Yildiz, J. Am. Chem. Soc. 135 (2013) 7909–7925.